Journal of Power Sources 240 (2013) 155–167

Contents lists available at SciVerse ScienceDirect

Journal of Power Sources

journal homepage: www.elsevier.com/locate/jpowsour

Numerical study of grain boundary effect on Li^+ effective diffusivity and intercalation-induced stresses in Li-ion battery active materials

Sangwoo Han [a], Jonghyun Park [a], Wei Lu [a,*], Ann Marie Sastry [b]

[a] Department of Mechanical Engineering, University of Michigan, Ann Arbor, MI 48109, USA
[b] Sakti3, Inc., Ann Arbor, MI 48108, USA

HIGHLIGHTS

- We modeled polycrystalline Li-ion battery active material particles in 3D.
- Developed a FEM approach to capture the effect of grain boundary on Li-ion diffusivity.
- Apparent diffusion coefficient increases with increasing grain boundary densities.
- Grain boundary lowers intercalation stress by reducing the concentration gradients.
- Capacity utilization improves in the presence of a grain boundary network.

GRAPHICAL ABSTRACT

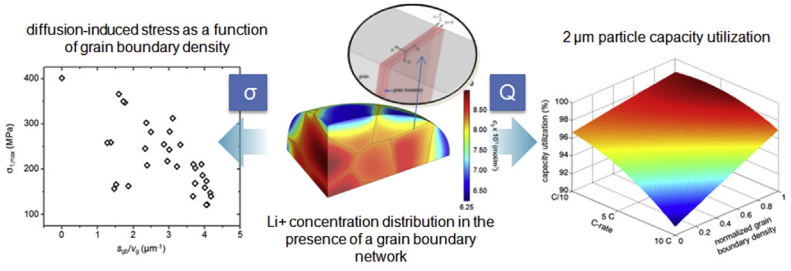

ARTICLE INFO

Article history:
Received 6 November 2012
Received in revised form
25 February 2013
Accepted 22 March 2013
Available online 4 April 2013

Keywords:
Grain boundary
Voronoi structure
Intercalation
Li-ion diffusion

ABSTRACT

We investigate the grain boundary effect on Li-ion diffusivity and intercalation-induced stress in a single-particle Li-ion cell. The measured activation energy for self-diffusion at the grain boundary is a fraction of that in the lattice due to the loosely packed structure, and this results in a diffusivity that is 3–16 orders of magnitude higher in the grain boundary than in the lattice. To study how grain boundaries affect Li-ion battery performance, grain boundaries are modeled inside ellipsoidal cathode ($LiMn_2O_4$) particles and placed under potentiodynamic and galvanostatic control simulations. A Voronoi grain distribution is employed in modeling grain boundaries. The grain boundary effect on Li-ion diffusivity is evaluated by computing an apparent diffusion coefficient from the cathode particles containing different grain boundary densities. It is shown that the apparent diffusion coefficient increases with increasing grain boundary densities. With enhanced Li-ion diffusivity, particles are found to have higher capacity utilizations, especially under high discharge C-rates. The inclusion of grain boundaries also lowered intercalation-induced stress by reducing the overall Li^+ concentration gradients developed within particles during cycling. However, as local Li^+ concentration distribution depends on grain boundary network geometries, intercalation-induced stress varied appreciably within the different grain boundary network geometries.

1. Introduction

An ideal secondary battery for hybrid electric vehicles would feature low cost, high gravimetric energy and power densities, an absence of thermal runaway for safety, and minimal capacity

* Corresponding author. Tel.: +1 734 647 7858; fax: +1 734 647 3170.
E-mail address: weilu@umich.edu (W. Lu).

0378-7753/$ – see front matter © 2013 Elsevier B.V. All rights reserved.
http://dx.doi.org/10.1016/j.jpowsour.2013.03.135

degradation. High gravimetric power density in particular allows for increased vehicle acceleration and a reduced battery charging time. The power performance of a lithium ion (Li-ion) secondary battery is primarily determined by Li-ion diffusivity in the host electrode materials. In the host electrode material, Li-ion diffusivity is influenced by intercalation-induced stress fields [1–4], phase boundary mobilities [5–7], and crystallographic defects [8,9]. Both thin-film and primary particle Li-ion active materials are polycrystalline materials, which are dense aggregates of single crystals joined by a network of interfacial crystallographic defects known as grain boundaries. It is widely recognized that the grain boundary network in these materials influence their properties, including transport properties. The more loosely packed structures of the grain boundaries result in a higher diffusivity compared to that inside the grain. For polycrystalline materials, the measured activation energy for self-diffusion at the grain boundary is only a fraction of that in the lattice, resulting in a diffusivity that is 3–16 orders of magnitude higher in the grain boundary than in the lattice [10–12]. These experiments have shown that as the average grain size is refined to nanoscale, the grain boundary increasingly dominates the transport properties.

To investigate the grain boundary effect on overall diffusivity, Fisher first modeled a single fast diffusing grain boundary embedded in a semi-infinite bulk of much lower diffusivity [13]. The model and its variants are today widely used in understanding grain boundary diffusion. For simplified polycrystalline geometries, where grain boundaries are lamellar [14] or square matrices [15,16], expressions for an effective diffusion coefficient have been formulated using rules-of-mixture or volumetric averages of the constituent diffusion coefficients. Although the rules-of-mixture method has also been used to study more complex structural effects such as grain size distributions [17] or triple junction densities [18], numerical methods such as molecular dynamics or the Monte Carlo method are more common in studying the effective diffusivity in the presence of grain boundaries. Moreover, effective diffusivities have been classified into different regimes of diffusion kinetics [19,20]. For example, based on the ordering of bulk diffusion length, grain boundary diffusion length, grain boundary thickness, and the average grain size, the overall diffusion kinetics may be determined by grain boundary diffusivity or a mixture of both bulk and grain boundary diffusivities.

Based on various experimental studies, the role of grain boundaries in Li-ion active materials has been postulated. For example, in a $LiCoO_2$ thin-film where grains are oriented in a preferred (0 0 3) direction that lithium ions have difficulty diffusing through, grain boundaries may facilitate lithium ions to diffuse into the bulk [21]. A study with *in situ* scanning probe microscopy (SPM) also showed that the formation of (LiF) particles at the grain boundaries lead to reduced lithium ion flux into the active material, as reflected on cyclic voltammograms [22]. Conversely, other studies suggest that grain orientations have a more significant influence on the overall Li-ion diffusivity than the grain boundary density, especially for materials with two dimensional lattice diffusion mechanisms such as $LiCoO_2$ [23] and V_2O_5 [24]. In one study, using the electrochemical strain microscopy (ESM) method, relatively higher Li^+ diffusivity was observed in certain grain facets and grain boundary-like features in a $LiCoO_2$ thin-film [25]. Another study showed that Sn-containing grain boundaries may be used as intercalation sites among inactive $SnMn_3C$ grains [26]; it demonstrates that grain boundaries may be utilized in controlling large volume expansion/contraction in metal anodes, which lead to energy capacity degradation. Indeed, many Li-ion active materials, including metal-alloys [27,28], $LiCoO_2$ [29], $LiMn_2O_4$ [30], and $LiFePO_4$ [31], undergo reversible lattice expansion during charging/discharging. Hence, internal strains/stresses may develop, leading to a gradual loss of energy capacity by dislocations, microcracks [29,31], or isolation of the active material from the current collector [32]. Several models have been developed to estimate the intercalation-induced stress in Li-ion active materials during charging/discharging [1–3]. These models show that intercalation-induced stress is roughly proportional to the concentration gradient developed in the particle. Because a grain boundary network can modify the concentration distribution within active materials, it would also affect intercalation-induced stress and its associated energy capacity degradation.

Although various postulations have been made in regards to the role of grain boundaries in Li-ion active materials, the effect of grain boundaries in Li-ion batteries has never been studied systematically. This is possibly due to difficulty in controlling the grain boundary density without affecting material phase and grain size/orientation distributions. Furthermore, in composite electrodes, the porosity can complicate the analysis. To study grain boundary effect on Li-ion battery performance, we model ellipsoidal cathode particles embedded with grain boundaries using a finite element method approach. By integrating a Fisher-type grain boundary model with a Li-ion stress-diffusion model, the role of grain boundary on overall Li^+ diffusivity, intercalation-induced stress, and energy capacity utilization is investigated. We have the following objectives:

1. To develop an electrochemical–mechanical model that considers grain boundaries in Li-ion active materials
2. To investigate the grain boundary effect on Li-ion battery performance including lithium ion diffusivity, intercalation-induced stress, and capacity utilization

2. Methods

To investigate grain boundary effect on overall lithium diffusivity as well as intercalation-induced stress, a Fickian diffusion equation coupled with a Hookean stress–strain constitutive equation was solved. Diffusion–stress coupling was achieved by including the elastic energy of the solute in the chemical potential [3,33,34].

Diffusion–stress model in the grain domain – Lithium ion diffusion is driven by the chemical potential gradient. For a given lithium ion concentration and hydrostatic stress gradients, the diffusion flux for a dilute or ideal system is given by Zhang et al. [3]

$$\mathbf{J}_g = -D_g\left(\nabla c_g - \frac{\Omega c_g}{RT}\nabla\sigma_h\right) \tag{1}$$

where subscript g indicates the grain or bulk domain, D_g is the diffusion coefficient, c_g is the concentration, Ω is partial molar volume, R is the universal gas constant, T is temperature, and σ_h is hydrostatic stress, defined as $\sigma_h = (\sigma_{11} + \sigma_{22} + \sigma_{33})/3$ (where σ_{ij} is the element in the stress tensor). Substituting Eq. (1) into the mass conservation equation, the following species transport equation in the grain domain was obtained

$$\frac{\partial c_g}{\partial t} + \nabla\cdot\left[-D_g\left(\nabla c_g - \frac{\Omega c_g}{RT}\nabla\sigma_h\right)\right] = 0. \tag{2}$$

In the cubic $Li_xMn_2O_4$ ($0 < x < 1$) phase, the lattice parameter of the host material was assumed to change linearly with the amount of ions inserted [35]; this results in intercalation-induced stresses. Therefore, the stress can be calculated using a thermal-analogy

stress model [3,36]. The stress–strain relation with the effect of intercalation is given by

$$\varepsilon_{ij} = \frac{1}{E}\left[(1+\nu)\sigma_{ij} - \nu\sigma_{kk}\delta_{ij}\right] + \frac{\Omega\Delta c_g}{3}\delta_{ij}, \tag{3}$$

where Δc_g is the concentration change of the diffusion species from the original stress-free value. Eqs. (2) and (3) are coupled through concentration, c_g, and stress, σ_h.

Li^+ transport in the grain boundary domain – Fisher grain boundary modeling [13,37] was adopted here. One assumption made in the model is that the concentration change across the grain boundary is negligible. Hence, the grain boundary domain can be modeled as a 2D surface embedded in 3D grain domains. In a finite element method, this assumption significantly reduces the computational cost because a high concentration of meshing near the very thin grain boundary can be avoided. Assumptions made in the grain boundary modeling are as follows:

i. Fick's laws are obeyed in the grain boundary domain
ii. Unlike in the grain domain, intercalation-induced stress is neglected in the grain boundary domain due to its amorphous nature and negligible associated volume expansion/contraction
iii. The grain boundary diffusion coefficient D_{gb} is isotropic and independent of concentration and time
iv. D_{gb} is greater than D_g
v. Concentrations and normal fluxes at the grain and grain boundary interface are continuous (i.e., no segregation effect)
vi. Concentration across the grain boundary is symmetrical on either side of the middle plane

An expression of species flux in the grain boundary domain is as follows

$$\mathbf{J}_{gb} = -D_{gb}\nabla c_{gb}(n,t_1,t_2,t). \tag{4}$$

The subscript gb denotes the grain boundary and t represents time. Here, the concentration gradient is decomposed into normal, n, and two tangential components, t_1 and t_2, relative to the middle plane of the grain boundary; hence, the gradient is taken as $\nabla = (\partial/\partial n, \partial/\partial t_1, \partial/\partial t_2)$. Conservation of mass in the grain boundary domain is expressed as

$$\frac{\partial c_{gb}}{\partial t} + \nabla\cdot\mathbf{J}_{gb} = 0. \tag{5}$$

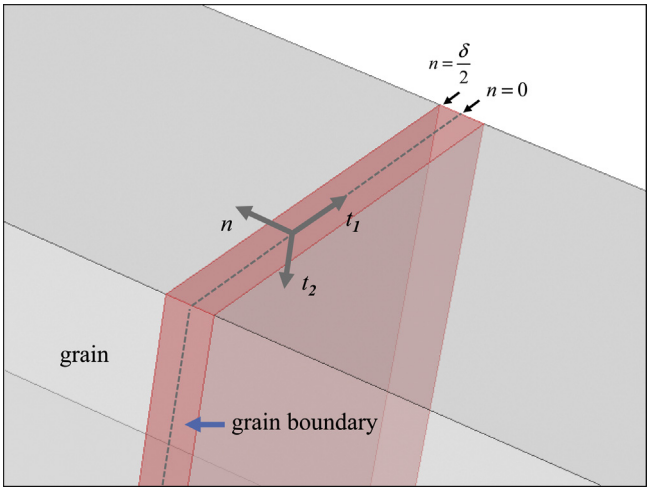

Fig. 1. A schematic diagram of a grain boundary embedded between two grains.

A simplified schematic diagram of the grain boundary between two grains is shown in Fig. 1, where the thickness of the grain boundary is δ. The model assumes that the concentration and normal fluxes at the grain/grain boundary interface are continuous, as described in Eqs. (6a) and (6b).

$$c_g(n,t_1,t_2,t) = c_{gb}(n,t_1,t_2,t) \quad n = \pm\delta/2 \tag{6a}$$

$$\mathbf{n}\cdot\mathbf{J}_g(n,t_1,t_2,t) = \mathbf{n}\cdot\mathbf{J}_{gb}(n,t_1,t_2,t) \quad n = \pm\delta/2 \tag{6b}$$

A Taylor series expansion of the grain boundary concentration with respect to $n = 0$ is written as

$$\begin{aligned} c_{gb}(n,t_1,t_2,t) &= c_{gb}(n,t_1,t_2,t)\big|_{n=0} + n\frac{\partial c_{gb}(n,t_1,t_2,t)}{\partial n}\Big|_{n=0} \\ &+ \frac{n^2}{2}\frac{\partial^2 c_{gb}(n,t_1,t_2,t)}{\partial n^2}\Big|_{n=0} \\ &+ \ldots + \frac{n^m}{m!}\frac{\partial^m c_{gb}(n,t_1,t_2,t)}{\partial n^m}\Big|_{n=0} \\ &\text{where } m = 1,2,3,\ldots \end{aligned} \tag{7}$$

Here it is assumed that the concentration across the grain boundary thickness is an even function about $n = 0$ due to symmetry. Because the first derivative of an even function evaluated at the point of symmetry is zero, all the odd functions in Eq. (7) are neglected. Taking a derivative with respect to n and neglecting third order and higher terms in Eq. (7), the following expression can be obtained.

$$\frac{\partial c_{gb}(n,t_1,t_2,t)}{\partial n} = n\frac{\partial^2 c_{gb}(n,t_1,t_2,t)}{\partial n^2}\Big|_{n=0}. \tag{8}$$

Eq. (8) evaluated at the grain/grain boundary interface $n = \pm\delta/2$ is:

$$\frac{\partial c_{gb}(n,t_1,t_2,t)}{\partial n}\Big|_{n=\pm\delta/2} = \pm\frac{\delta}{2}\frac{\partial^2 c_{gb}(n,t_1,t_2,t)}{\partial n^2}\Big|_{n=0}. \tag{9}$$

Combining Eq. (9) with Eqs. 4, 5, and 6(b), then solving in terms of $\mathbf{J}_g$, yields:

Table 1
Parameters and $LiMn_2O_4$ material properties.

Symbol and unit	Name	Value
E (GPa)	Young's modulus	100
ν	Poisson's ratio	0.3
D_g ($m^2\ s^{-1}$)	Bulk or lattice diffusion coefficient	7.08×10^{-15} (Ref. [1])
Ω ($m^3\ mol^{-1}$)	Partial molar volume	3.497×10^{-6}
c_{max} (mol m^{-3})	$LiMn_2O_4$ stoichiometric maximum concentration	2.29×10^4
V (V)	Applied ramp potential	3.5–4.3 V with 1 mV s^{-1} sweep rate
U (V)	Open circuit potential	Curve fit (Ref. [51])
c_l (mol m^{-3})	Electrolyte Li^+ salt concentration	1000
β (–)	Symmetry factor	0.5
k ($m^{5/2}\ s^{-1}\ mol^{-1/2}$)	Reaction rate constant	1.9×10^{-9} (Ref. [50])
F (C mol^{-1})	Faraday's constant	96487
T (K)	Temperature	300
R (J $mol^{-1}\ K^{-1}$)	Universal gas constant	8.314

$$\mathbf{n}\cdot\mathbf{J}_g\big|_{n=+\delta/2} = -\frac{\delta}{2}\frac{\partial c_{gb}(t_1,t_2,t)}{\partial t} + \frac{\delta}{2}D_{gb}\nabla_t^2 c_{gb}(t_1,t_2,t), \text{ and} \tag{10a}$$

$$\mathbf{n}\cdot\mathbf{J}_g\big|_{n=-\delta/2} = \frac{\delta}{2}\frac{\partial c_{gb}(t_1,t_2,t)}{\partial t} - \frac{\delta}{2}D_{gb}\nabla_t^2 c_{gb}(t_1,t_2,t). \tag{10b}$$

The right-hand side of Eq. (10) is all quantities on the middle plane of the grain boundary ($n = 0$) and $\nabla_t = (\partial/\partial t_1, \partial/\partial t_2)$. Thus the grain boundary becomes a 2D object. Although Fig. 1 shows a grain boundary with a thickness δ, in the actual model, grain boundaries are modeled as 2D surfaces between two grains without geometric thickness. Eqs. (10a) and (10b) may be considered as a boundary condition for $\mathbf{J}_g$ at the grain/grain boundary interface. Prior to implementing the boundary condition, Eqs. (10a) and (10b) are converted to a boundary weak form as follows:

$$\mathbf{n}\cdot\mathbf{J}_g\big|_{n=+\delta/2} = -\int_S w\frac{\delta}{2}\frac{\partial c_{gb}}{\partial t}dS + \int_S wD_{gb}\frac{\delta}{2}\nabla_t^2 c_{gb}dS, \text{ and} \tag{11a}$$

$$\mathbf{n}\cdot\mathbf{J}_g\big|_{n=-\delta/2} = \int_S w\frac{\delta}{2}\frac{\partial c_{gb}}{\partial t}dS - \int_S wD_{gb}\frac{\delta}{2}\nabla_t^2 c_{gb}dS. \tag{11b}$$

In Eq. (11), S represents the grain boundary interface domain, and w is the weighting function. Noting that

$$wD_{gb}\nabla_t^2 c_{gb} = -D_{gb}\nabla_t w\cdot\nabla_t c_{gb} + \nabla_t\cdot\left(wD_{gb}\nabla_t c_{gb}\right), \tag{12}$$

Eqs. (11a) and (11b) can be re-written as

$$\mathbf{n}\cdot\mathbf{J}_g\big|_{n=+\delta/2} = -\frac{\delta}{2}\int_S w\frac{\partial c_{gb}}{\partial t}dS - \frac{\delta}{2}\int_S D_{gb}\nabla_t w\cdot\nabla_t c_{gb}dS + \frac{\delta}{2}\int_S \nabla_t\cdot\left(wD_{gb}\nabla_t c_{gb}\right)dS, \text{ and} \tag{13a}$$

$$\mathbf{n}\cdot\mathbf{J}_g\big|_{n=-\delta/2} = \frac{\delta}{2}\int_S w\frac{\partial c_{gb}}{\partial t}dS + \frac{\delta}{2}\int_S D_{gb}\nabla_t w\cdot\nabla_t c_{gb}dS - \frac{\delta}{2}\int_S \nabla_t\cdot\left(wD_{gb}\nabla_t c_{gb}\right)dS. \tag{13b}$$

By the Divergence theorem, the last terms in Eqs. (13a) and (13b) can be re-written as

$$\int_S \nabla_t\cdot\left(wD_{gb}\nabla_t c_{gb}\right)dS = \int_l wD_{gb}\nabla_t c_{gb}\cdot\mathbf{m}dl, \tag{14}$$

where $\mathbf{m}$ is the normal direction of the edge curve of the grain boundary surface. Assuming that the net flux along the edges of the grain boundary is zero, the above term was neglected. Hence, the final boundary weak form of the flux at the grain/grain boundary interface is:

$$\mathbf{n}\cdot\mathbf{J}_g\big|_{n=+\delta/2} = -\frac{\delta}{2}\int_S w\frac{\partial c_{gb}}{\partial t}dS - \frac{\delta}{2}\int_S D_{gb}\nabla_t w\cdot\nabla_t c_{gb}dS, \text{ and} \tag{15a}$$

$$\mathbf{n}\cdot\mathbf{J}_g\big|_{n=-\delta/2} = \frac{\delta}{2}\int_S w\frac{\partial c_{gb}}{\partial t}dS + \frac{\delta}{2}\int_S D_{gb}\nabla_t w\cdot\nabla_t c_{gb}dS. \tag{15b}$$

Using COMSOL Multiphysics, Eqs. (2) and (15) for lithium transport in the grain and grain boundary domains were solved using a general PDE and a weak boundary form module, respectively. Eq. (3) for intercalation-induced stress was solved using a general PDE module.

Electrochemical kinetics under galvanostatic and potentiodynamic controls – In this study, a cell consisting of a micron-scale single-particle positive electrode with lithium metal negative electrode was modeled. The positive electrode was isotropic cubic-phase $Li_xMn_2O_4$ ($0 \le x \le 1$) prolate spheroids containing grain boundaries. During charging, species are oxidized at the positive electrode, and lithium ions are extracted. During discharging, species are reduced at the positive electrode, and lithium ions are inserted. The reactions for the $LiMn_2O_4$ positive electrode are

$$LiMn_2O_4 \Leftrightarrow Li_{1-x}Mn_2O_4 + xLi^+ + xe^-. \tag{16}$$

Under a galvanostatic control, a constant diffusion flux $\mathbf{J}$ was applied at the particle surface,

$$\mathbf{n}\cdot\mathbf{J} = i_n/F, \tag{17}$$

where F is Faraday's constant, and the discharge/charge current density i_n was determined based on the C-rate;

Under a potentiodynamic control, the diffusion flux boundary condition at the particle surface was determined by the Butler–Volmer equation [38],

$$\mathbf{n}\cdot\mathbf{J} = \frac{i_n}{F} = \frac{i_0}{F}\left\{\exp\left[\frac{(1-\beta)F}{RT}\eta\right] - \exp\left[-\frac{\beta F}{RT}\eta\right]\right\}. \tag{18}$$

Here i_0 is the exchange current density, η is surface overpotential, and β is a symmetry factor which represents the fraction

Table 2
Representative grain sizes in Li-ion particles and thin-films.

Active material	Configuration	Synthesis method	Primary particle size	Grain size	Ref.
$LiMn_2O_4$	Particles	Spray pyrolysis	~1.1 μm	25 nm	Zhang et al. [45]
$LiMn_2O_4$	Particles	Calcination	~3 μm	<100 nm	He et al. [44]
$Li[Ni_{1/3}Co_{1/3}Mn_{1/3}]O_2$	Particles	Spray pyrolysis	~500 nm	10–50 nm	Park et al. [46]
$LiCoO_2$	Particles	Unknown	>10 μm	~0.5–5 μm	Wilson et al. [47]

Active material	Configuration	Synthesis method	Grain size	Ref.
$LiMn_2O_4$	Thin film	PLD	200–300 nm	Shin et al. [48]
$LiCoO_2$	Thin film	RF sputtering	~10–100 nm	Bates et al. [49]
$LiFePO_4$	Thin film	PLD	~200 nm	Lu et al. [50]
$LiNi_{0.5}Mn_{0.5}O_2$	Thin film	PLD	100–200 nm	Xia et al. [51]

Table 3
Simulation input variables and their levels.

Potentiodynamic control	Values
D_{gb}/D_g	10^3 and 10^4
Ellipsoidal particle semi-axis dimensions ($a \times b \times c$, μm)	1.2 × 1.2 × 2.0
Number of crystallites/grains	3–15
Grain boundary thickness, δ (nm)	0, 2, 4, 8, and 16
Galvanostatic control	**Values**
D_{gb}/D_g	10^3
Ellipsoidal particle semi-axis dimensions ($a \times b \times c$, μm)	Set 1: 1.2 × 1.2 × 2.0 Set 2: 3.0 × 3.0 × 5.0
Number of crystallites/grains	3–15
Grain boundary thickness, δ (nm)	0 and 5

of the applied potential that promotes the cathodic reaction. The exchange current density, i_0, is given by

$$i_0 = Fkc_l^{1-\beta}(c_{max} - c_s)^{1-\beta}c_s^{\beta}, \quad (19)$$

where c_l is the concentration of lithium ion in the electrolyte, c_s is the Li^+ concentration at the particle surface, $(c_{max} - c_s)$ is the concentration of available vacant sites on the surface ready for lithium intercalation (or equivalently, the difference between stoichiometric maximum concentration and current concentration on the surface of the electrode), and k is a reaction rate constant [39]. The surface overpotential, η, is the difference between the applied potential at the solid phase surface, V, and the equilibrium open circuit potential, U:

$$\eta = V - U. \quad (20)$$

As for the applied potential, V, a linear ramp potential with a sweep rate of 1.0 mV s^{-1} was used. An experimental fit of the open circuit potential [40] (OCP) as a function of state-of-charge (SOC) x in $Li_xMn_2O_4$ was used in the simulation. The $LiMn_2O_4$ spinel material properties and simulation parameters are listed in Table 1. In all simulations, the lattice diffusion coefficient was assumed to be isotropic and constant irrespective of the SOC.

Generation of particles with grain boundaries – Polycrystalline primary particles in composite electrodes are agglomerated using polymeric binders [e.g., polyvinylidene fluoride (PVDF)] and carbon-based conductive additives (e.g., carbon black, graphite) to form secondary particles. Reported secondary particle sizes range from 6 to 60 μm [41–43]. Primary particle sizes vary with synthesis techniques and range from 0.3 to 4 μm [41,43,44]. Primary particles as well as thin-film electrodes consist of crystalline grains, and their sizes also depend on synthesis methods. An annealing step in the synthesis process is often performed to yield a desired phase, but it may also be used to control grain sizes. Typical grain sizes in primary particles and thin-film electrodes are shown in Table 2. Grain sizes range from 25 nm to >1 μm in primary particles [44–47] and from 10 to 300 nm in thin-film electrodes [48–51]. As for the grain boundary thickness, a thickness of 4–25 nm has been observed for metal oxides including Al_2O_3 [52], $MgAl_2O_4$ spinel [53], and Mg_2GeO_4 spinel [54], under high resolution transmission electron microscopy (HRTEM). Grain boundary diffusivity is typically several orders of magnitude greater than in the lattice [10–12]. The grain boundary diffusivities for transition metal oxides such as Cr_2O_3 [55], Fe_3O_4 [56], and ZnO [57] typically range 3–7 orders of magnitude greater than the lattice diffusion. For the $LiMn_2O_4$ spinel, a grain boundary diffusion coefficient measured by secondary ion mass spectroscopy (SIMS) was approximately 3–4 orders greater than in the lattice [58]. In representing grain size distributions in polycrystalline materials, various distributions such as a monodispersed Tetrakaidecahedra distribution [17], a spread Johnson-Mehl distribution [17,59], and a nearly log-normal Voronoi distribution [17,59] have been used. In this study, a Voronoi distribution that consists of convex polyhedron grains was used. To generate Voronoi polycrystalline particles, the Multi Parametric Matlab Toolbox [60] was used. Each Voronoi structure was generated by specifying a number of grains. The particles containing grain boundary structures were then imported to COMSOL Multiphysics to run simulations. A prolate ellipsoid particle shape was used in all simulations. Assuming symmetry about x, y, and z, only one-eighth of the particle was used in the simulation.

Potentiodynamic control simulation input and output parameters – In the potentiodynamic control simulation, intercalation-induced stress and lithium ion diffusivity were investigated as a function of grain boundary network structure, grain boundary Li^+ diffusivity, and grain boundary thickness. A total of 31 prolate ellipsoidal particles with identical dimensions were used in the simulation. The 31 particles consisted of 1 particle without grain boundary and 30 particles with a unique grain boundary network structure. To control grain boundary Li^+ diffusivity, the ratio of grain boundary-to-bulk diffusion coefficient, D_{gb}/D_g, varied between 10^3 and 10^4, while the bulk diffusion coefficient, D_g, remained fixed. Finally, grain boundary thickness, δ, varied from 2 nm to 16 nm. Input variables and their levels used in the potentiodynamic control simulation are summarized in Table 3. In quantifying the grain

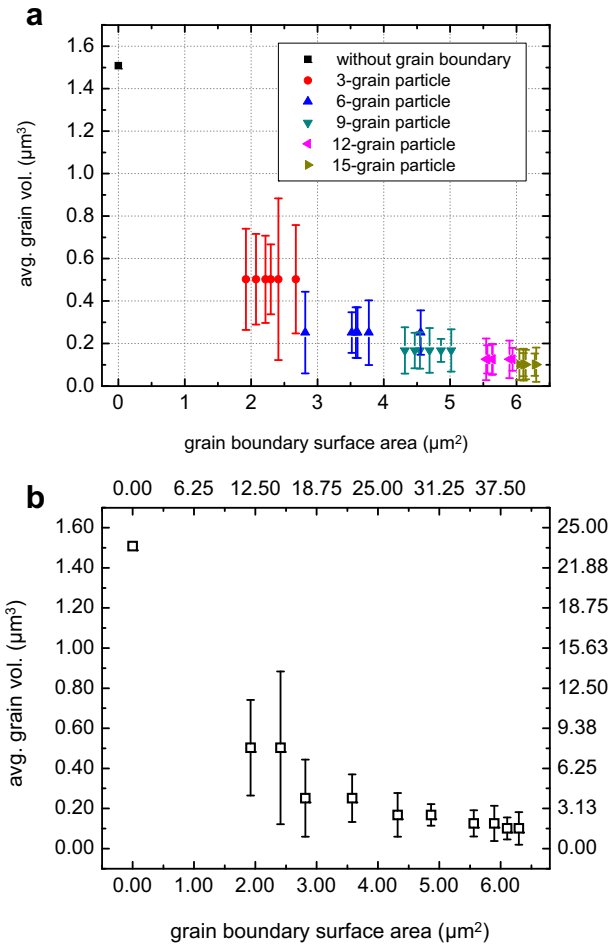

Fig. 2. A summary of the average grain size and the grain boundary surface area for polycrystalline particles generated for: (a) the potentiodynamic control simulation and (b) the galvanostatic control simulation.

boundary effect on intercalation-induced stress, the maximum principal stress was evaluated. To quantify relative changes in the overall diffusivity, an apparent diffusion coefficient was computed based on the peak current from the potentiodynamic control simulation. Assuming that the intercalation/de-intercalation process is fully reversible, an apparent diffusion coefficient was computed based on the cyclic voltammetry (CV) diffusion equation [61,62], as shown in Eq. (21); the equation is valid when $T = 300$ K.

$$D_{\mathrm{Li}} = \left(\frac{i_{\mathrm{p}}/v^{1/2}}{(2.68 \times 10^5) n^{3/2} a c_{\mathrm{o}}^{0}} \right)^2. \tag{21}$$

In Eq. (21), i_{p} is the peak current, v is the linear potential sweep rate, n is the number of moles of electrons transferred in the reaction, a is the electrode surface area, and c_{o}^{0} is the initial lithium ion concentration in the fully lithiated system, which is 2.29 mol m^{-3} for $LiMn_2O_4$.

Galvanostatic control simulation input and output parameters – To test the particle size and the grain boundary effects on the capacity utilization, two sets of particles with different sizes were tested. The particle dimensions were identical within each set. The first set of particles consisted of 1 particle without grain boundary and 10 particles with unique Voronoi grain boundary network structures. The second set of particles consisted of the same 11 particles in the first set but the dimension was scaled up by a factor of 2.5 in all *x*-, *y*-, and *z*-directions. The grain boundary structures within the particles scaled accordingly. A fixed grain boundary thickness of $\delta = 5$ nm and a grain boundary-to-lattice diffusion coefficient ratio, $D_{\mathrm{gb}}/D_{\mathrm{g}} = 10^3$ were used in both sets. With various C-rates, each particle was galvanostatically discharged from 4.3 V to 3.5 V, or equivalently until the lithium ion concentration at a particle surface reached $c_{\max}$. Input variables and their levels used in the galvanostatic control simulation are summarized in Table 3. The output discharge capacity utilization, denoted as Γ, was calculated by dividing the amount of lithium inserted at the particle surface over the maximum amount of lithium ions a particle can contain, or

$$\Gamma = \frac{1}{V_{\mathrm{p}} \cdot c_{\max}} \int_0^{t_f} \left(\int_S \frac{i_n}{F} \mathrm{d}S \right) \mathrm{d}t. \tag{22}$$

Here V_{p} represents particle volume, t_{f} is time when the lithium ion concentration at the particle surface reached 3.5 V or $c_{\max}$, and S is the particle surface.

3. Results and discussion

Generated grain boundary network structures – The average grain sizes and associated standard deviations *vs*. grain boundary surface areas for the polycrystalline particles generated for the simulation are shown in Fig. 2. Fig. 2a and b corresponds to the particles used in the potentiodynamic control simulation and the galvanostatic control simulation, respectively. In Fig. 2, the particles have the same size but different number of grains. Thus for those particles with the same number of grains, their average grain sizes are the same. The upper and lower bounds show the standard deviation associated with different grain volumes in each particle. Because the specified number of grains was a multiple of three, the grain boundary surface areas are not evenly populated, as seen in Fig. 2a. Six grain arrangements are considered for each total number of grains in a particle, so Fig. 2a shows results for a total of 31 particles. In the galvanostatic control simulation, two sets of particles were used. In Fig. 2b, the bottom abscissa and the left ordinate correspond to the first set of particles, and the top abscissa and the right ordinate correspond to the second set of particles. Because the second set of particles was created by scaling up particles in the first set by a factor of 2.5 in *x*-, *y*-, and *z*-direction, the grain boundary network structures between the two sets were conserved. After scaling, the surface area and the volume of each grain increased by a factor of 2.5^2 and 2.5^3, respectively. However, the grain boundary surface area-to-particle volume ratio, $s_{\mathrm{gb}}/v_{\mathrm{g}}$, was reduced by a factor of 2.5 after the scaling. The grain sizes in the generated polycrystalline particles are comparable to those grain sizes estimated from cross-sectioned images of $LiCoO^2$ composite electrodes [47].

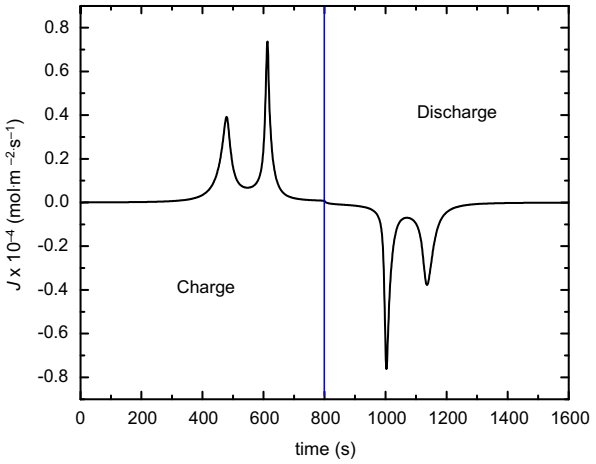

Fig. 3. A time history of reaction flux during the potentiodynamic control simulation for a particle without grain boundary.

The grain boundary effect on intercalation-induced stress – Particles were first charged and then discharged with a potential sweep rate of 1.0 mV s^{-1} in the potential range between 3.5 V and 4.3 V. Fig. 3 shows the time history of reaction flux at the particle surface for a particle without grain boundary. During charging the flux is negative, as lithium ions are extracted; during discharging the flux is positive, as lithium ions are inserted. Fig. 3 also shows two flux peaks during each half cycle, similar to results from simulations [39] and experiments [63]. According to the Bulter–Volmer electrochemical kinetics shown in Eq. (18), the reaction flux is a function of surface overpotential η and exchange current density i_0. The exchange current density, i_0, depends on the type of electrolyte, temperature, and nature of the electrode surface [38]. A reaction with a large value of i_0 is often described as fast. Also in Eq. (18), the current density varies linearly with η for small values of η, and exponentially with η for large values of η. If the surface overpotential is plotted as a function of time, it would peak twice during each half cycle because the applied potential increases linearly while $LiMn_2O_4$ OCP contains two plateaus. Hence, the reaction flux peaks shown in Fig. 3 are largely determined by the thermodynamic property of $LiMn_2O_4$. In addition, the exchange current density may shift the time location of the peak slightly. During charging, lithium ions are extracted from the particle surface. Therefore, during charging the outer layer becomes lithium-poor relative to the inner core, creating a concentration gradient. As lithium ions are extracted from the surface, the outer layer contracts and applies a compressive (negative) stress to the inner core. However, the outer layer cannot contract freely due to the inner core. As a result, it experiences a tensile (positive) stress. During discharging, the outer layer expands as lithium ions are inserted from the particle surface. In the case of discharging, the outer layer can expand relatively freely, and therefore, experiences almost no stress. The inner core, on the other hand, is pulled by the expanding outer layer and experiences tensile (positive) stress.

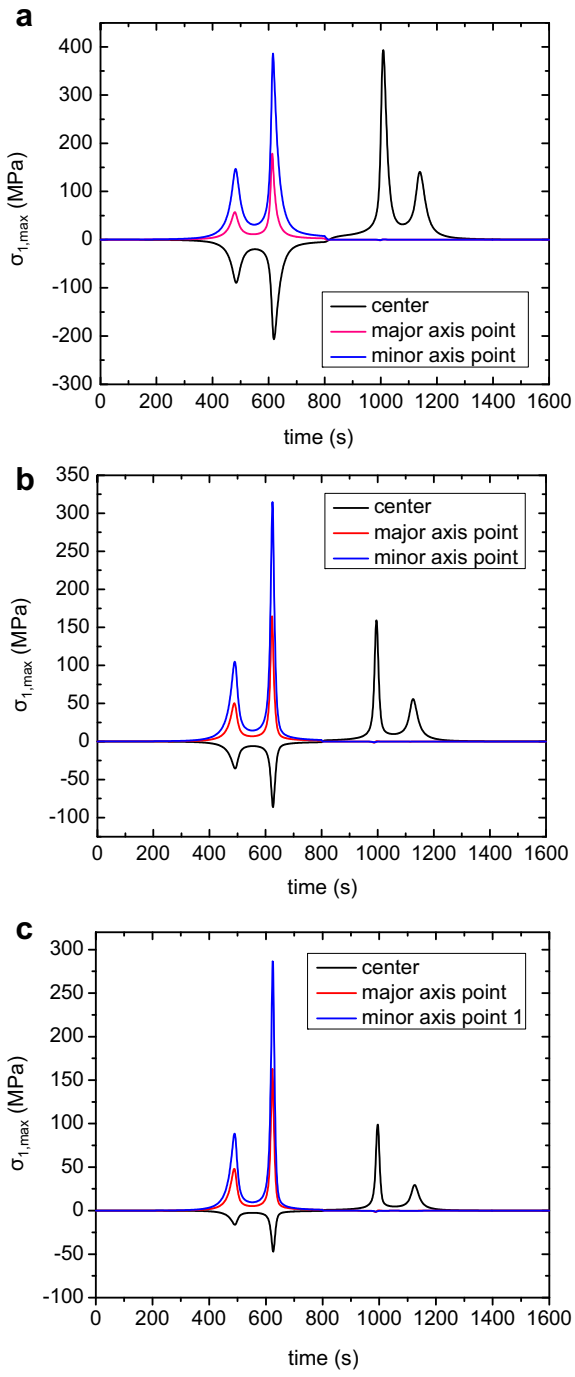

Fig. 4. A time history of intercalation-induced stress at three specific points (particle center and two surface points located on minor and major ellipsoidal axes) during the potentiodynamic control simulation for: (a) a particle without grain boundary, (b) a particle with a grain boundary network structure with $D_{gb}/D_g = 10^3$, and (c) a particle with the same grain boundary network structure as in (b) but with $D_{gb}/D_g = 10^4$.

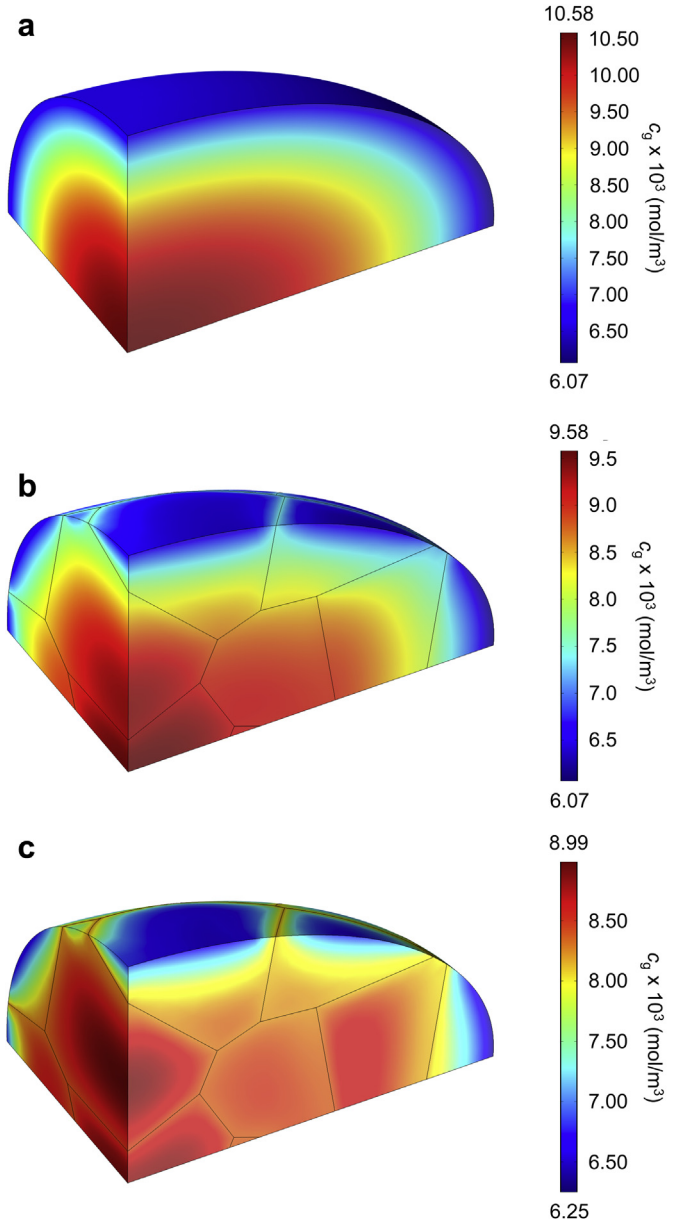

Fig. 5. Lithium ion concentration distribution when intercalation-induced stress is at its maximum during charge for the same three particles in Fig. 4: (a) the particle without grain boundary, (b) the particle with a grain boundary network structure for $D_{gb}/D_g = 10^3$, and (c) the particle with the same grain boundary network structure as in (b) but for $D_{gb}/D_g = 10^4$.

Fig. 4 shows the time history of the maximum first principal stress during charging and discharging for particles with and without grain boundaries. The profiles shown in Fig. 4a correspond to a particle without grain boundary and the profiles shown in Fig. 4b and c correspond to particles with grain boundaries. Grain boundary structures and cycling conditions in Fig. 4b and c were identical. The only different condition between Fig. 4b and c was the diffusion coefficient ratio, D_{gb}/D_g. Ratios of 10^3 and 10^4 were used in Fig. 4b and c, respectively. The three stress profiles in each figure correspond to the particle center point and two surface points located on the minor and major axes. During charging, the two surface points undergo tensile stress, while the center point undergoes compressive stress. During discharging, the surface experiences almost no stress, while the inner core experiences tensile stress. In the presence of grain boundaries, lithium ions can be inserted into and extracted from the particle inner core more rapidly through grain boundaries, lowering the overall concentration gradient as well as intercalation-induced stress during both charging and discharging. With increasing grain boundary Li^+ diffusion coefficient, intercalation-induced stress is reduced even further, as seen in Fig. 4c. Fig. 5 shows the lithium ion concentration distribution at the point in time when the first principal stress is at its maximum during charge. Fig. 5a–c corresponds to the particles in Fig. 4a–c, respectively. Lithium ion concentrations being higher

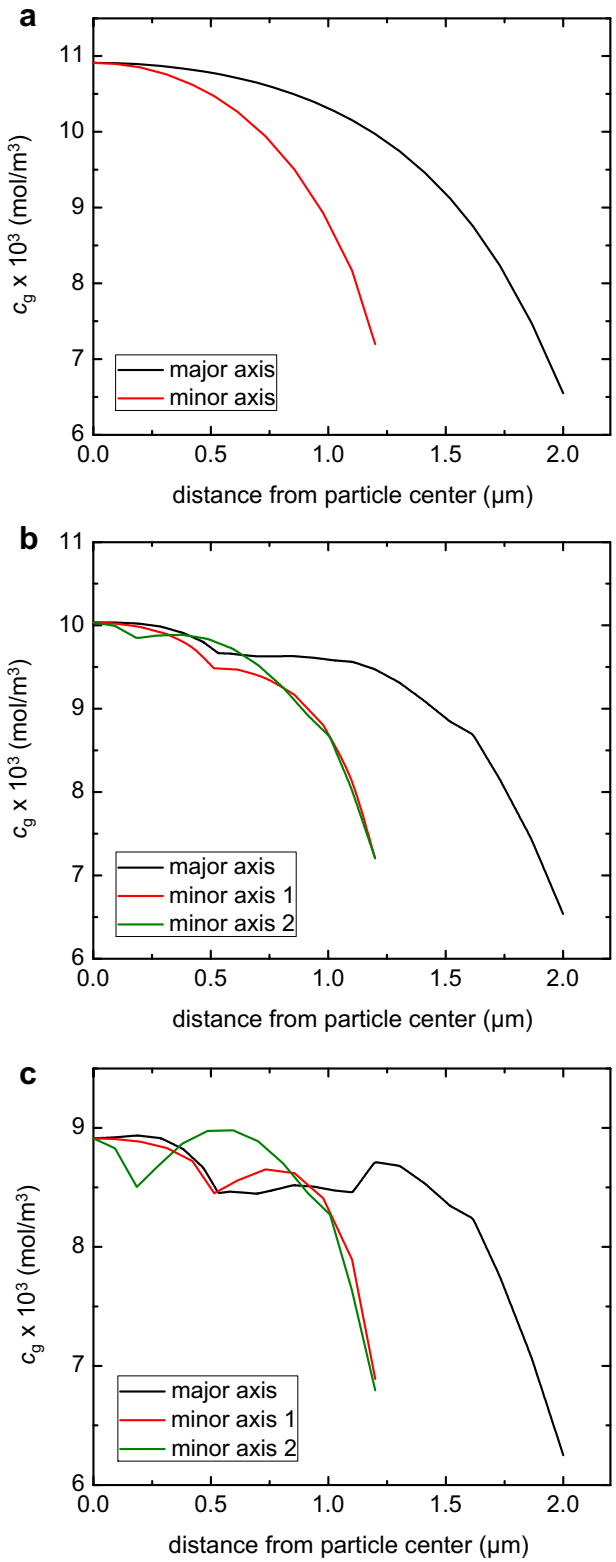

Fig. 6. Lithium ion concentration profiles along the minor axes when intercalation-induced stress is at its maximum during charge for the same three particles in Fig. 4: (a) the particle without grain boundary, (b) the particle with a grain boundary network structure for $D_{gb}/D_g = 10^3$, and (c) the particle with the same grain boundary network structure as in (b) but for $D_{gb}/D_g = 10^4$.

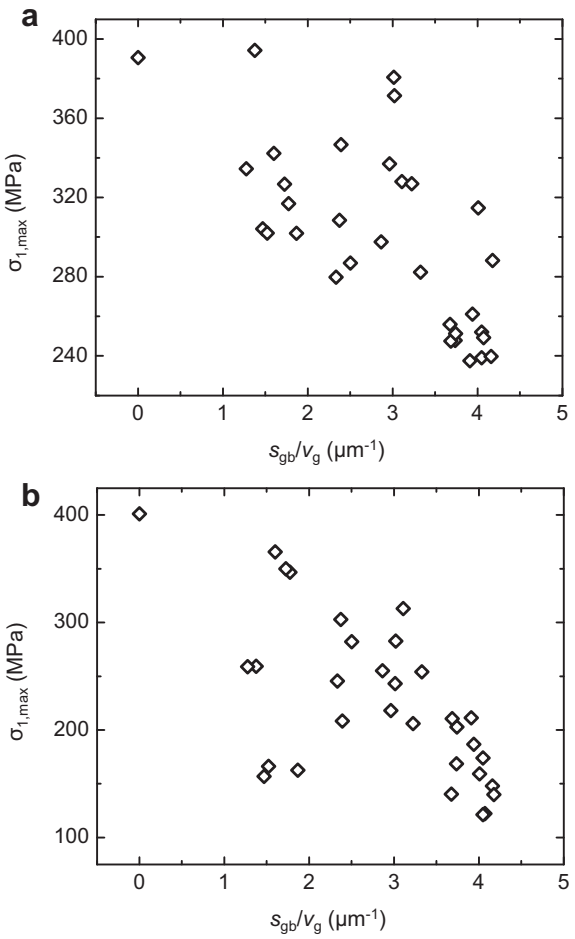

Fig. 7. A summary of the maximum intercalation-induced stress in the 31 particles observed during the potentiodynamic control simulation: (a) during charge and (b) during discharge.

along the grain boundaries on and near the particle surface can be clearly seen in Fig. 5b and c. For the three particles represented in Fig. 4, the maximum first principal stress experienced at the surface point located on the minor axis is higher than at the surface point located on the major axis. This is due to a higher net Li^+ concentration gradient in the minor axis than in the major axis. Fig. 6 shows the lithium ion concentration profiles along the minor and major axes when the intercalation-induced stress is at a maximum during charging. Fig. 6a–c corresponds to the same particles in Fig. 4a–c, respectively. For the particle without grain boundary, as represented in Fig. 6a, the difference between the lithium ion concentration at the particle center and at the surface points in the minor and major axes are 3945 mol cm^{-3} and 4145 mol cm^{-3}, respectively. However, the minor axis length is 1.2 μm, whereas the major axis length is 2.0 μm. Hence, the net concentration gradient along the minor axis is approximately more than 50% higher than along the major axis, which leads to higher tensile stress. Moreover, the concentration decrease is monotonic along the minor and major axes for the particle without grain boundary. For particles with grain boundary, however, the concentrations along minor and major axes do not decrease monotonically, as shown in Fig. 6b and c. Instead, the concentration increases slightly whenever a grain boundary is encountered. This concentration increase becomes pronounced when D_{gb}/D_g increases from 10^3 to 10^4, as shown in Fig. 6b and c. When the diffusion coefficient ratio D_{gb}/D_g increases from 10^3 to 10^4, the net concentration gradient along the minor axis reduces by 29%, and the maximum principal stress decreases by 9%. For an ideal or dilute solid solution system where the activity coefficient of diffusing species is independent of concentration,

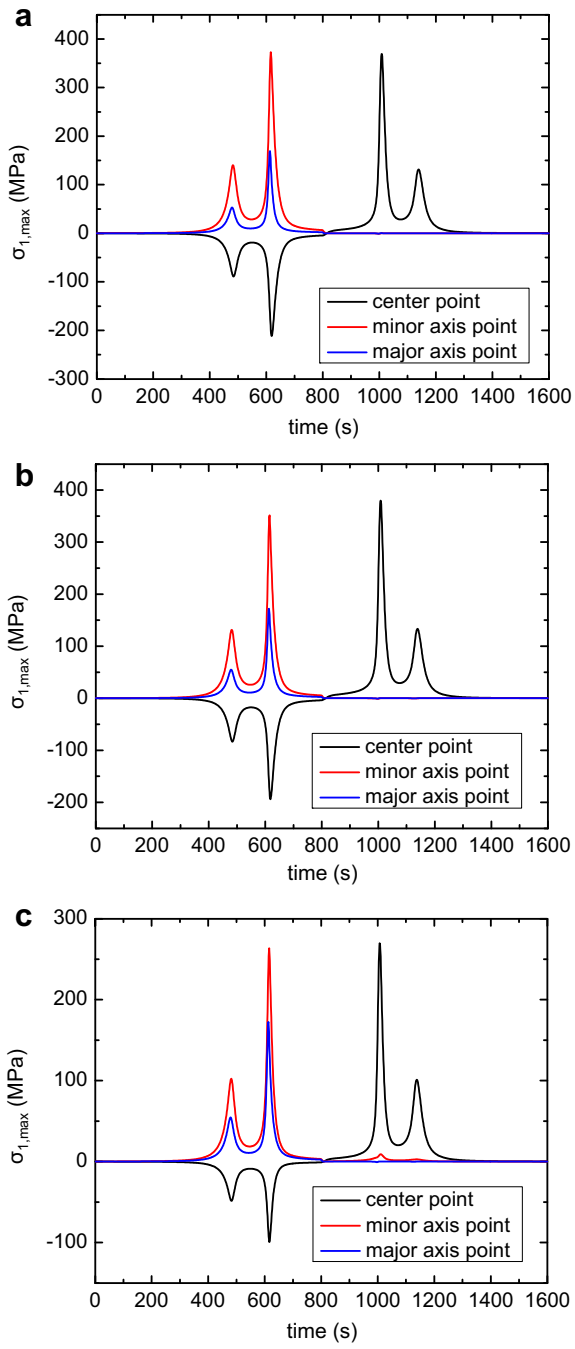

Fig. 8. Intercalation-induced stress profiles at three specific points (particle center and two surface points located on minor and major ellipsoidal axes) for three particles containing a single grain boundary with the same surface area oriented at different angles: (a) case 1 – a grain boundary oriented away from the particle center, (b) case 2 – a grain boundary oriented in parallel with the major axis, and (c) case 3 – a grain boundary oriented such that it passes through the particle center.

intercalation- or diffusion-induced stress always enhances Li-ion diffusivity [3,34], as described in Eq. (1). Although high diffusivity of grain boundaries may reduce the enhanced diffusivity caused by intercalation-induced stress, the high diffusivity of grain boundaries itself results in even higher overall diffusivity.

Potentiodynamic control simulations were performed on 31 particles, and the maximum first principal stress induced during charging and discharging is summarized in Fig. 7a and b, respectively. A fixed grain boundary thickness of $\delta = 8$ nm was used for

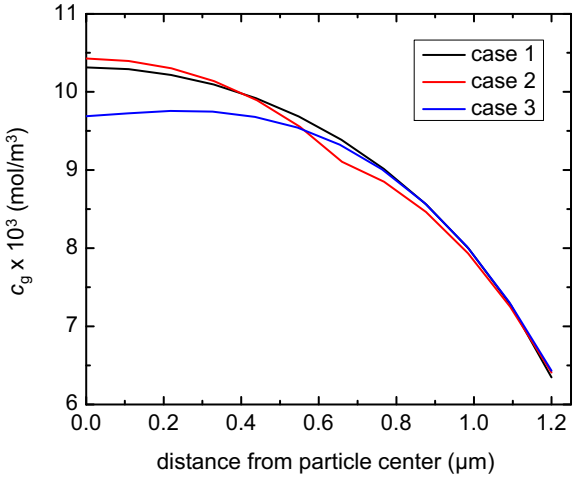

Fig. 9. Lithium ion concentration profiles along the minor axes when intercalation-induced stress is at its maximum during charging for the same three particles containing a single grain boundary: case 1 – a grain boundary oriented away from the particle center, case 2 – a grain boundary oriented in parallel with the major axis, and case 3 – a grain boundary oriented such that it passes through the particle center.

particles with grain boundaries. The maximum first principal stress generally decreases with an increasing grain boundary surface area-to-lattice volume ratio, s_{gb}/v_g. However, it does not show a strong correlation with the s_{gb}/v_g ratio (although discussed later, the apparent diffusion coefficients show a stronger correlation with increasing s_{gb}/v_g ratio). Assuming a linear relationship between $\sigma_{1,max}$ and s_{gb}/v_g, adjusted-R^2 values are 0.46 and 0.40 for charge and discharge data set, respectively. The intercalation-induced stress is primarily determined by the lithium ion concentration distribution inside particles. As seen in Fig. 6b and c, the lithium ion concentration distribution may be modified significantly with the grain boundary network structure and the grain boundary-to-bulk diffusion coefficient ratio. To investigate the grain boundary network structure effect on intercalation-induced stress, three particles containing a single grain boundary surface with the same surface area were considered. In the first case (case 1), a grain boundary bisects a particle away from the particle center; in the second case (case 2), a grain boundary is parallel to the long axis; in the last case (case 3), a grain boundary passes through the particle center. All three cases contained a single grain boundary with an identical grain boundary surface area of 1.315 μm^2 ($s_{gb}/v_g = 0.872$ μm^{-1}). The time histories of intercalation-induced stress at the particle center point and two surface points located on the major and minor axes are shown in Fig. 8. In all three cases, the maximum stress during charging occurs at the surface point located on the minor axis. During charging, the maximum intercalation-induced stress for the three cases is 372 MPa for case 1, 368 MPa for case 2, and 330 MPa for case 3. During discharging, the maximum intercalation-induced stress at the particle center is 369 MPa for case 1, 380 MPa for case 2, and 270 MPa for case 3. Fig. 9 shows the concentration along the minor axis for the three cases when intercalation-induced stress is at their maximum during charge. Also Fig. 10 shows the 3D lithium ion concentration distribution for the three particles when intercalation-induced stress is at their maximum during charging. The three cases demonstrate that an orientation of a grain boundary itself can have an influence on the maximum intercalation-induced stress by modifying Li^+ concentration gradients within particles.

The grain boundary effect on Li^+ diffusivity – Fig. 11 shows the computed apparent diffusion coefficients as a function of grain

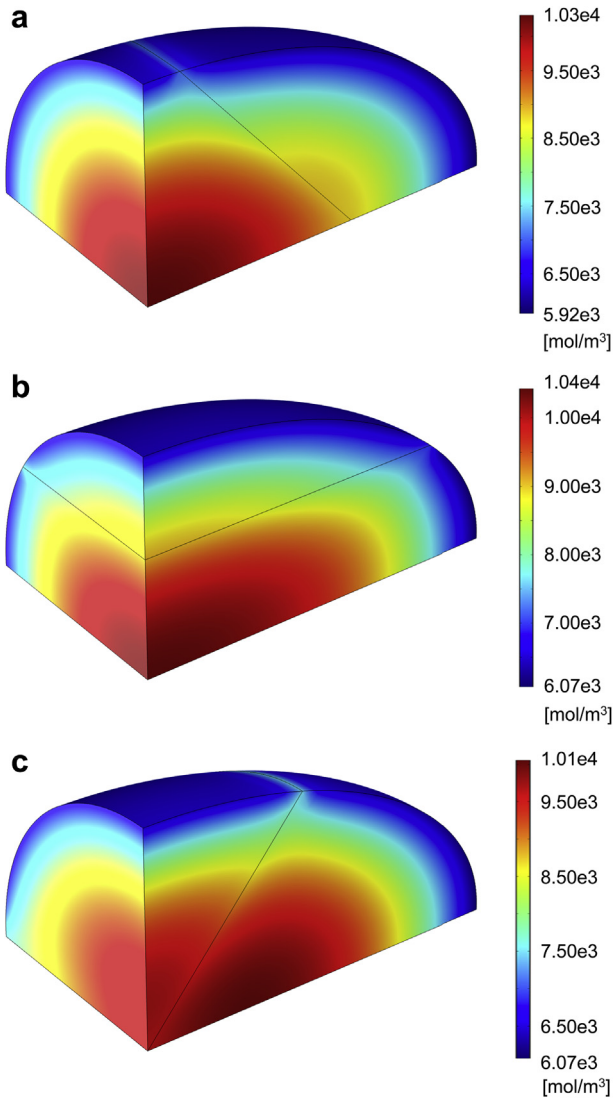

Fig. 10. 3D surface plots of lithium ion concentrations when the maximum intercalation-induced stress has reached its maximum during charge for the three particles containing a single grain boundary: (a) case 1 particle, (b) case 2 particle, and (c) case 3 particle.

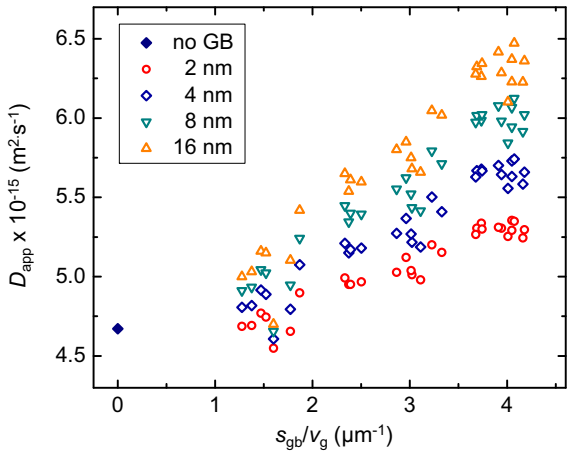

Fig. 11. A summary of apparent diffusion coefficients based on the second reaction flux peak during discharge for the 31 particles with a fixed diffusion coefficient ratio, $D_{gb}/D_g = 1000$ but varying grain boundary thicknesses.

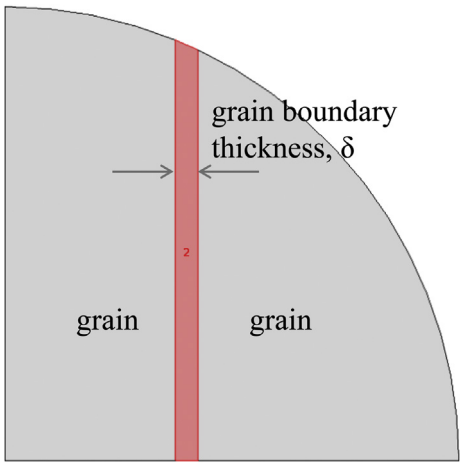

Fig. 12. A schematic diagram of a 2D particle containing a single grain boundary.

surface-area-to-particle-volume ratios s_{gb}/v_g for various grain boundary thicknesses. The apparent diffusion coefficients are based on the first reaction flux peak during discharge. For a given grain boundary thickness, the apparent diffusion coefficient increases almost linearly in the tested s_{gb}/v_g range. Assuming a linear relationship between D_{app} and s_{gb}/v_g, adjusted-R^2 values do range between 0.91 and 0.92 for all grain boundary thicknesses. Moreover, as the grain boundary thickness increases, apparent diffusion coefficients rise faster with s_{gb}/v_g. This is because in the governing equation for the lithium ion transport in the grain boundary domain, as described in Eq. (15), the grain boundary thickness, δ, and the grain boundary diffusion coefficient, D_{gb}, are multiplied together and input as a constant. Therefore, the two effects are coupled in the model. For example, a twofold increase in the grain boundary thickness yields the same results as a twofold increase in the grain boundary diffusion coefficient.

To investigate the individual effect of grain boundary diffusion coefficient and the thickness on diffusivity, a 2D model containing an actual grain boundary thickness was considered. The shape of the cathode particle was a circle with 2 μm radius and assuming symmetry about x- and y-axes, only a quarter of the circle was modeled. A schematic image of the cathode particle is shown in Fig. 12. In parallel with the 3D model, the 2D model included the plane thermal-analogy intercalation-induced stress in the grain domain only. Two sets of potentiodynamic control simulations were performed with the 2D model. In the first set, a grain boundary thickness was fixed while the grain boundary diffusion coefficient varied, while in the second set, the grain boundary diffusion coefficient was fixed while the grain boundary thickness varied. The design of computation is summarized in Table 4 and the same material properties in Table 1 were used.

Apparent Li^+ diffusion coefficients evaluated from the two sets of simulations are summarized in Fig. 13. Using Eq. (22), diffusion coefficients are evaluated based on the first reaction flux peak during charging. In the first set, D_{app} increases with increasing D_{gb}/D_g ratio although the D_{app} quickly approaches a saturation limit. In

Table 4
Input variables for the 2D model.

	Fixed δ	D_{gb}/D_g levels				
Set 1	$\delta = 4$ nm	1000	2000	4000	8000	16,000
	Fixed D_{gb}/D_g	δ levels				
Set 2	$D_{gb}/D_g = 1000$	4 nm	8 nm	16 nm	32 nm	64 nm

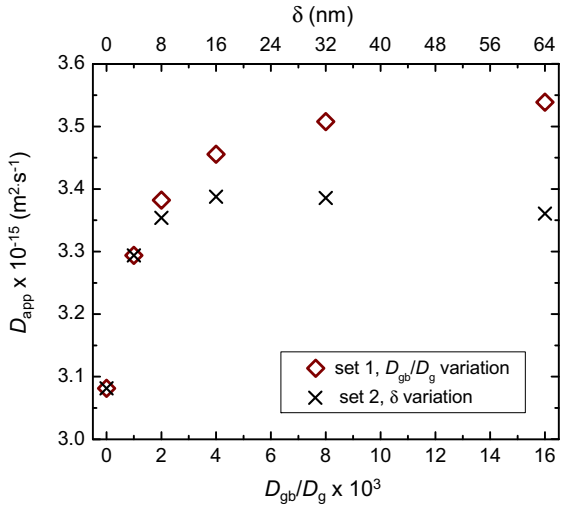

Fig. 13. A summary of apparent diffusion coefficients based on the first reaction flux peak during charging from the 2D simulation.

the second set, in contrast, D_{app} peaks when $\delta = 16$ nm then decreases with a further increase in the grain boundary thickness. Because D_{app} is proportional to the reaction flux squared, the reaction flux contributions from grain and grain boundary domains are calculated separately and shown in Fig. 14.

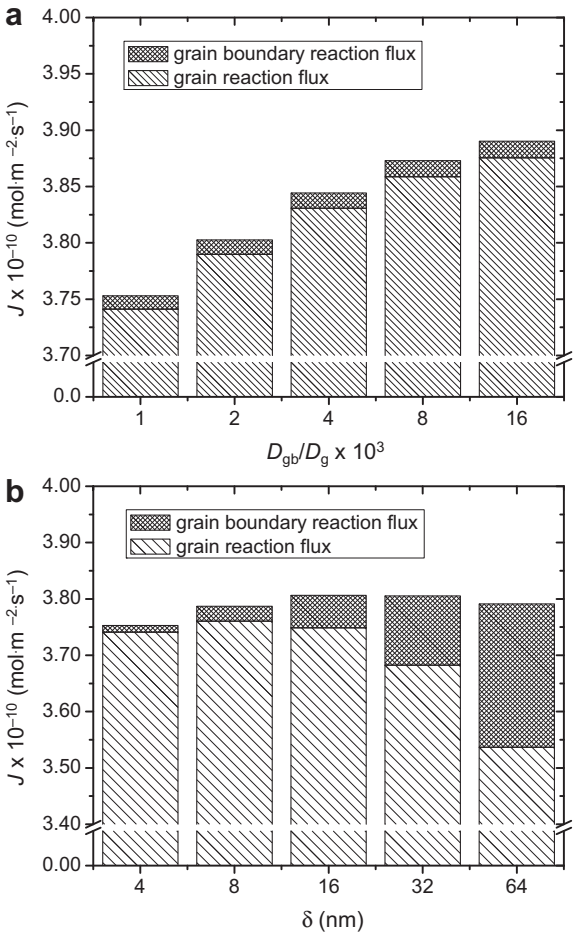

Fig. 14. Reaction flux contributions from bulk and grain boundary domains: (a) set 1 – where the grain boundary diffusivity is a variable and (b) set 2 – where the grain boundary thickness is a variable.

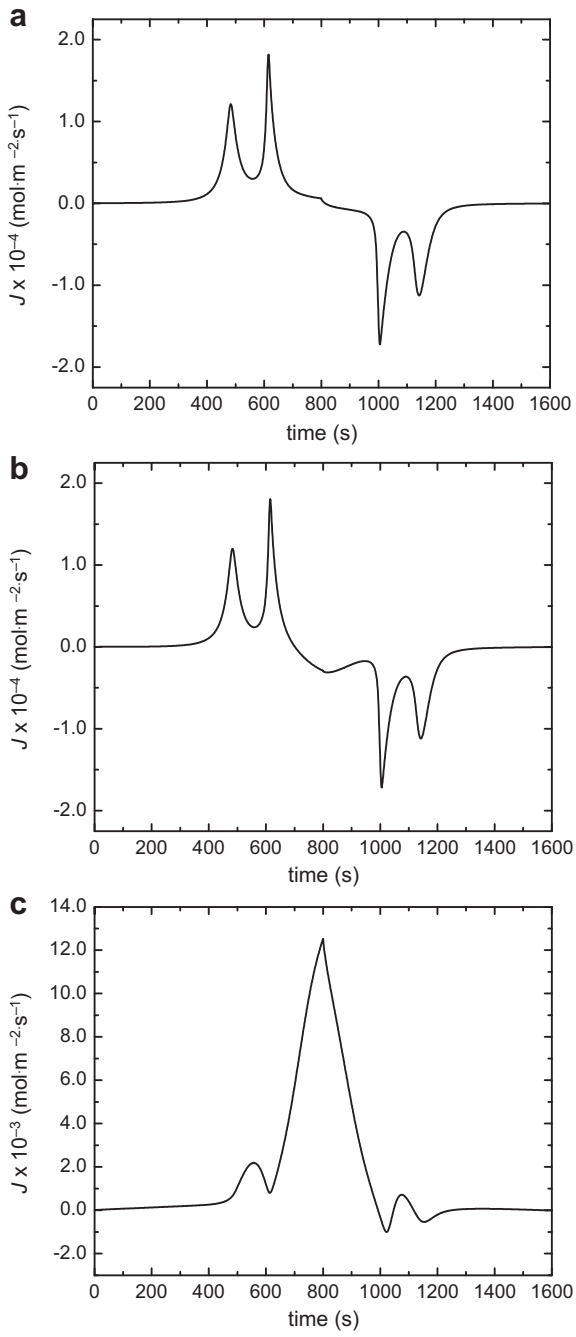

Fig. 15. A time history of the reaction flux from a 2D particle with $D_{gb}/D_g = 10^3$ and $\delta = 16$ nm: (a) total reaction flux, (b) reaction flux from the bulk/grain domain, and (c) reaction flux from the grain boundary domain.

In the first set, as grain boundary diffusion coefficient increases, the species flux contribution from the grain boundary remains almost the same whereas the reaction flux contribution from the grain increases, as shown in Fig. 14a. With higher grain boundary diffusion coefficient, lithium ions can travel faster along a grain boundary. Due to the condition that the concentration at the grain/grain boundary interface needs to be equal, the increase in the grain boundary diffusion coefficient induces higher concentration gradient as well as species flux in the grain domain. Although not shown here, the magnitude of the concentration gradient increases in the grain domain with increasing D_{gb}. This implies that the diffusivity in the grain boundary affects the diffusivity in the bulk

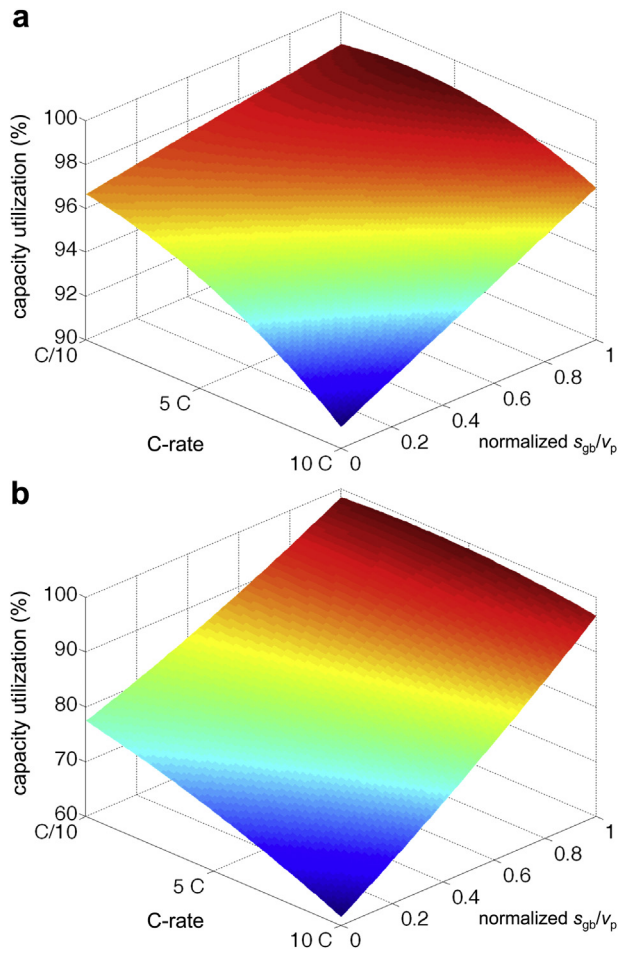

Fig. 16. Second order surface fits of capacity utilization results from particles under the galvanostatic control simulation: (a) particles with a dimension of $2 \times 1.2 \times 1.2\ \mu m^3$ and (b) particles with a dimension of $5 \times 3 \times 3\ \mu m^3$.

domain. The reason for the reaction flux contribution from the grain boundary remaining almost the same is as follows. Owing to the relatively higher lithium ion diffusivity in the grain boundary, a higher concentration of lithium ions is developed in the grain boundary region compared to neighboring bulk domain. The OCP is a function of lithium ion concentration. Due to the concentration difference, given an applied potential, the surface overpotential and the time location of the reaction flux peaks are different at the grain/electrolyte interface and the grain boundary/electrolyte interface. As an example, Fig. 15a shows the time history of the total reaction flux during charge/discharge for a case where $D_{gb}/D_g = 1000$ and $\delta = 16$ nm. The reaction flux at the grain/electrolyte and grain boundary/electrolyte interfaces are plotted separately in Fig. 15b and c, respectively. The first reaction flux peak at the grain–electrolyte occurs at $t = 483$ s, whereas the first reaction flux peak at the grain boundary–electrolyte interface occurs at $t = 558$ s. Because the apparent diffusion coefficient is evaluated based on the overall reaction flux peak, the reaction flux at the grain boundary–electrolyte interface is evaluated before its first peak is reached. This illustrates why the reaction flux contribution from the grain boundary does not increase with increasing grain boundary diffusion coefficient.

In the second set, the reaction flux contribution from the grain boundary is approximately doubled as δ becomes a two fold, as shown in Fig. 14b. In contrast, the reaction flux contribution from the grain increases slightly from $\delta = 4$ to $\delta = 8$ then decreases with a further increase in the grain boundary thickness. There are two competing factors that affect species flux. The first is the concentration gradient and the second is the domain size. With increasing grain boundary thickness, the magnitude of the concentration gradient increases just like in the first set of simulations. On the other hand, the total number of lithium ions flowing from the grain decreases with shrinking domain size. Hence, the reaction flux contribution in the grain domain increases only to a certain grain boundary thickness threshold.

Grain boundary effect on capacity utilization – The two sets of particles were discharged with various C-rates, and their capacity utilizations were computed according to Eq. (22). The resulting capacity utilizations as a function of C-rates and grain boundary-surface-area-to-particle-volume ratio, s_{gb}/v_g, were then fitted with a second order polynomial surface. The surface fits shown in Fig. 16a and b correspond to the first and second sets of particles, respectively. The s_{gb}/v_g ratio is normalized to its highest value. The two sets of particles show decreasing capacity utilization with increasing C-rates and decreasing s_{gb}/v_g ratio. At C/5 and lower, the capacity utilization is 97% or higher for all particles in both sets, including the particles without grain boundary. In the first set, the particle without a grain boundary retains capacity utilizations of 94% and 90% at C-rates of 5 C and 10 C, respectively. In the presence of the grain boundary, the average capacity utilization increases to 98% for 5 C and 96% for 10 C. In contrast, in the second set, the capacity utilization of the particle without grain boundary is 74% and 61% at C-rates of 5 C and 10 C, respectively. The decrease in the capacity utilization in the second set is due to increased particle volume by a factor of 2.5^3, i.e. larger diffusion distance to reach the particle center. In the presence of the grain boundary, the average capacity utilization increases to 85% for 5 C and 73% for 10 C. The marginal increase in the capacity utilization is appreciably greater in the second set despite that the grain boundary-surface-area-to-particle-volume, s_{gb}/v_g, is 2.5^2 lower compared to the smaller particles in the first set. Nonetheless, the overall trend of increasing capacity with grain boundary surface-area-to-particle-volume is consistent with increasing apparent diffusion coefficient with surface area-to-particle volume. Although capacity utilization tends to increase with grain boundary density, the particle with the highest s_{gb}/v_g ratio does not achieve the maximum capacity utilization. For example, with equal particle sizes, a particle with $s_{gb}/v_g = 4.0\ \mu m^{-1}$ achieves a capacity utilization of 89% while a particle with $s_{gb}/v_g = 10.4\ \mu m^{-1}$ achieves a capacity utilization of 84% when the C-rate is 5 C. This shows that a grain boundary network structure can influence capacity utilization. To improve Li-ion battery power performance in composite electrodes, the average particle sizes have been reduced by various synthesis techniques and mechanical means. However, increasing electrode–electrolyte interfacial density may lead to higher capacity degradation due to increased side reactions [64,65] and dissolution [66]. To suppress such phenomena, surface coating on Li-ion cathodes has often been performed [67,68]. The same effect may be achieved without coating but by utilizing the grain boundary network structure. As grain boundaries can have an influence on Li^+ transport, intercalation-induced stress, and even phase transformation sites, grain boundary engineering of Li-ion active materials may be an alternative avenue to enhance Li-ion battery performance.

4. Conclusions

The grain boundary effect on intercalation-induced stress, Li^+ diffusivity, and capacity utilization was investigated by implementing 2D Voronoi grain boundary structures embedded inside 3D $LiMn_2O_4$ particles. The main cause of intercalation-induced stress inside a single cathode particle is the lithium ion

concentration gradient developed during charging and discharging. The net concentration gradient was reduced with the inclusion of high diffusion grain boundary pathways. Consequently, the maximum intercalation-induced stress also decreased. Although the maximum intercalation-induced stress tended to diminish with increasing grain boundary density, the actual stress level exhibited a high dependence on individual grain boundary network geometries. While intercalation-induced stress tended to be reduced in the presence of the grain boundary, the computed apparent diffusion coefficient, as well as the capacity utilization, increased. As discussed above, grain boundaries may have a significant role in determining the performance of Li-ion secondary batteries. Moreover, grain boundaries are inevitable in commercially available Li-ion active materials. For these reasons, grain boundaries should be controlled during synthesis to enhance the performance of Li-ion secondary batteries.

Acknowledgments

The authors would like to acknowledge the support of the GM/UM Advanced Battery Coalition for Drivetrains.

References

[1] J. Christensen, J. Newman, Journal of the Electrochemical Society 153 (6) (2006) A1019–A1030.
[2] H. Haftbaradaran, J. Song, W.A. Curtin, H. Gao, Journal of Power Sources 196 (1) (2011) 361–370.
[3] X. Zhang, W. Shyy, A.M. Sastry, Journal of the Electrochemical Society 154 (10) (2007) A910–A916.
[4] J. Park, W. Lu, A.M. Sastry, Journal of the Electrochemical Society 158 (2) (2011) A201–A206.
[5] C.S. Wang, U.S. Kasavajjula, P.E. Arce, Journal of Physical Chemistry C 111 (2007) 16656–16663.
[6] Y.J. Zhu, C.S. Wang, Journal of Physical Chemistry C 114 (6) (2010) 2830–2841.
[7] N. Meethong, Y.H. Kao, M. Tang, H.Y. Huang, W.C. Carter, Y.M. Chiang, Chemistry of Materials 20 (19) (2008) 6189–6198.
[8] R. Malik, D. Burch, M. Bazant, G. Ceder, Nano Letters 10 (10) (2010) 4123–4127.
[9] S. Adams, R.P. Rao, Solid State Ionics 184 (1) (2011) 57–61.
[10] J. Horvath, R. Birringer, H. Gleiter, Solid State Communications 62 (5) (1987) 319–322.
[11] T. Mutschele, R. Kirchheim, Scripta Metallurgica 21 (2) (1987) 135–140.
[12] Y.R. Kolobov, G.P. Grabovetskaya, M.B. Ivanov, A.P. Zhilyaev, R.Z. Valiev, Scripta Materialia 44 (6) (2001) 873–878.
[13] J.C. Fisher, Journal of Applied Physics 22 (1) (1951) 74–77.
[14] E.W. Hart, Acta Metallurgica 5 (10) (1957), 597.
[15] I.V. Belova, G.E. Murch, Journal of Physics and Chemistry of Solids 64 (5) (2003) 873–878.
[16] I.V. Belova, G.E. Murch, Nanodiffusion 19 (2004) 25–33.
[17] Y. Chen, C.A. Schuh, Journal of Applied Physics 101 (6) (2007).
[18] Y. Chen, C.A. Schuh, Scripta Materialia 57 (3) (2007) 253–256.
[19] L.G. Harrison, Transactions of the Faraday Society 57 (8) (1961) 1191.
[20] Y. Mishin, C. Herzig, Materials Science and Engineering A – Structural Materials Properties Microstructure and Processing 260 (1–2) (1999) 55–71.
[21] H. Xia, L. Lu, Electrochimica Acta 52 (24) (2007) 7014–7021.
[22] Y.S. Cohen, D. Aurbach, Electrochemistry Communications 6 (6) (2004) 536–542.
[23] W.S. Kim, Journal of Power Sources 134 (1) (2004) 103–109.
[24] S.C. Mui, J. Jasinski, V.J. Leppert, M. Mitome, D.R. Sadoway, A.M. Mayes, Journal of the Electrochemical Society 153 (7) (2006) A1372–A1377.
[25] N. Balke, S. Jesse, A.N. Morozovska, E. Eliseev, D.W. Chung, Y. Kim, L. Adamczyk, R.E. Garcia, N. Dudney, S.V. Kalinin, Nature Nanotechnology 5 (10) (2010) 749–754.
[26] L.Y. Beaulieu, D. Larcher, R.A. Dunlap, J.R. Dahn, Journal of the Electrochemical Society 147 (9) (2000) 3206–3212.
[27] U. Kasavajjula, C.S. Wang, A.J. Appleby, Journal of Power Sources 163 (2) (2007) 1003–1039.
[28] W.J. Zhang, Journal of Power Sources 196 (1) (2011) 13–24.
[29] H.F. Wang, Y.I. Jang, B.Y. Huang, D.R. Sadoway, Y.T. Chiang, Journal of the Electrochemical Society 146 (2) (1999) 473–480.
[30] M.R. Lim, W.I. Cho, K.B. Kim, Journal of Power Sources 92 (1–2) (2001) 168–176.
[31] D.Y. Wang, X.D. Wu, Z.X. Wang, L.Q. Chen, Journal of Power Sources 140 (1) (2005) 125–128.
[32] R. Kostecki, F. McLarnon, Electrochemical and Solid State Letters 7 (10) (2004) A380–A383.
[33] F.Q. Yang, Materials Science and Engineering A – Structural Materials Properties Microstructure and Processing 409 (1–2) (2005) 153–159.
[34] J. Chenminli, R.F. Mehl, Metallurgical Transactions A – Physical Metallurgy and Materials Science 9 (10) (1978) 1353–1380.
[35] W.I.F. David, M.M. Thackeray, L.A. Depicciotto, J.B. Goodenough, Journal of Solid State Chemistry 67 (2) (1987) 316–323.
[36] S. Prussin, Journal of Applied Physics 32 (10) (1961) 1876–1881.
[37] D. Gryaznov, J. Fleig, J. Maier, Solid State Sciences 10 (6) (2008) 754–760.
[38] J. Newman, K.E. Thomas-Alyea, Electrochemical Systems, third ed., John Wiley & Sons, Inc., New Jersey, 2004.
[39] D. Zhang, B.N. Popov, R.E. White, Journal of the Electrochemical Society 147 (3) (2000) 831–838.
[40] M. Doyle, J. Newman, A.S. Gozdz, C.N. Schmutz, J.M. Tarascon, Journal of the Electrochemical Society 143 (6) (1996) 1890–1903.
[41] N. Yabuuchi, Y. Koyama, N. Nakayama, T. Ohzuku, Journal of the Electrochemical Society 152 (7) (2005) A1434–A1440.
[42] T.H. Cho, S.M. Park, M. Yoshio, T. Hirai, Y. Hideshima, Journal of Power Sources 142 (1–2) (2005) 306–312.
[43] M. Higuchi, K. Katayama, Y. Azuma, M. Yukawa, M. Suhara, Journal of Power Sources 119 (2003) 258–261.
[44] X.M. He, J.J. Li, Y. Cai, C.Y. Jiang, C.R. Wan, Materials Chemistry and Physics 95 (1) (2006) 105–108.
[45] L.Q. Zhang, T. Yabu, I. Taniguchi, Materials Research Bulletin 44 (3) (2009) 707–713.
[46] S.H. Park, C.S. Yoon, S.G. Kang, H.S. Kim, S.I. Moon, Y.K. Sun, Electrochimica Acta 49 (4) (2004) 557–563.
[47] J.R. Wilson, J.S. Cronin, S.A. Barnett, S.J. Harris, Journal of Power Sources 196 (7) (2011) 3443–3447.
[48] D.W. Shin, J.W. Choi, J.P. Ahn, W.K. Choi, Y.S. Cho, S.J. Yoon, Journal of the Electrochemical Society 157 (5) (2010) A567–A570.
[49] J.B. Bates, N.J. Dudney, B.J. Neudecker, F.X. Hart, H.P. Jun, S.A. Hackney, Journal of the Electrochemical Society 147 (1) (2000) 59–70.
[50] Z.G. Lu, H. Cheng, M.F. Lo, C.Y. Chung, Advanced Functional Materials 17 (18) (2007) 3885–3896.
[51] H. Xia, L. Lu, M.O. Lai, Electrochimica Acta 54 (25) (2009) 5986–5991.
[52] D.R. Clarke, Journal of the American Ceramic Society 70 (1) (1987) 15–22.
[53] G.D. West, J.M. Perkins, M.H. Lewis, Journal of Materials Science 39 (22) (2004) 6687–6704.
[54] C. Dupas-Bruzek, T.N. Tingle, H.W. Green, N. Doukhan, J.C. Doukhan, Physics and Chemistry of Minerals 25 (7) (1998) 501–514.
[55] A.C.S. Sabioni, A.M. Huntz, F. Silva, F. Jomard, Materials Science and Engineering A – Structural Materials Properties Microstructure and Processing 392 (1–2) (2005) 254–261.
[56] A. Atkinson, Solid State Ionics 12 (March 1984) 309–320.
[57] H. Haneda, I. Sakaguchi, A. Watanabe, T. Ishigaki, J. Tanaka, Journal of Electroceramics 4 (1999) 41–48.
[58] T. Okumura, T. Fukutsuka, Y. Uchimoto, N. Sakai, K. Yamaji, H. Yokokawa, Journal of Power Sources 189 (1) (2009) 643–645.
[59] A. Thorvaldsen, Acta Materialia 45 (2) (1997) 587–594.
[60] I. f. Automatik, Multi Parametric Toolbox (MPT). http://control.ee.ethz.ch/~mpt/ (accessed 3.08.11).
[61] R.P. Frankenthal, I. Shain, Journal of the American Chemical Society 78 (13) (1956) 2969–2973.
[62] A.J. Bard, L.R. Faulkner, Electrochemical Methods: Fundamentals and Applications, second ed., John Wiley & Sons, Inc., 2001.
[63] I. Uchida, H. Fujiyoshi, S. Waki, Journal of Power Sources 68 (1) (1997) 139–144.
[64] J. Vetter, P. Novak, M.R. Wagner, C. Veit, K.C. Moller, J.O. Besenhard, M. Winter, M. Wohlfahrt-Mehrens, C. Vogler, A. Hammouche, Journal of Power Sources 147 (1–2) (2005) 269–281.
[65] M. Holzapfel, A. Wursig, W. Scheifele, J. Vetter, P. Novak, Journal of Power Sources 174 (2) (2007) 1156–1160.
[66] S.J. Wen, T.J. Richardson, L. Ma, K.A. Striebel, P.N. Ross, E.J. Cairns, Journal of the Electrochemical Society 143 (6) (1996) L136–L138.
[67] L.J. Fu, H. Liu, C. Li, Y.P. Wu, E. Rahm, R. Holze, H.Q. Wu, Solid State Sciences 8 (2) (2006) 113–128.
[68] C. Li, H.P. Zhang, L.J. Fu, H. Liu, Y.P. Wu, E. Ram, R. Holze, H.Q. Wu, Electrochimica Acta 51 (19) (2006) 3872–3883.